

PAPER

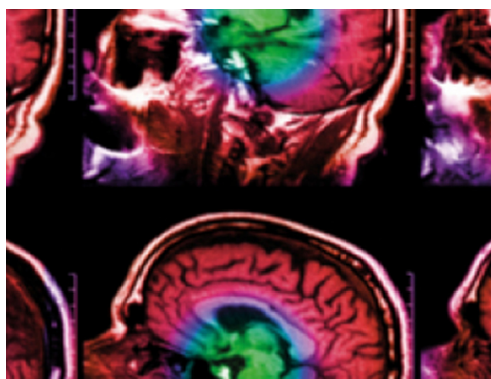
Organ dose calculator for diagnostic nuclear medicine patients based on the ICRP reference voxel phantoms and biokinetic models

To cite this article: Daphnée Villoing *et al* 2023 *Biomed. Phys. Eng. Express* **9** 015004

You may also like

- [Gut transfer and doses from environmental plutonium and americium](#)
John D Harrison
- [Lustrum - a trip to the Netherlands](#)
Colin Partington and John Jackson
- [SRP Meeting: Internal Dosimetry \(The British Library, 23 October 2002\)](#)
Penny Giorgio

View the [article online](#) for updates and enhancements.



IPEM | IOP

Series in Physics and Engineering in Medicine and Biology

Your publishing choice in medical physics,
biomedical engineering and related subjects.

Start exploring the collection—download the
first chapter of every title for free.

Biomedical Physics & Engineering Express



PAPER

Organ dose calculator for diagnostic nuclear medicine patients based on the ICRP reference voxel phantoms and biokinetic models

RECEIVED
13 June 2022REVISED
21 October 2022ACCEPTED FOR PUBLICATION
23 November 2022PUBLISHED
2 December 2022

Daphnée Villoing , Tae-Eun Kwon , Elisa Pasqual , Cari M Kitahara and Choonsik Lee

Division of Cancer Epidemiology and Genetics, National Cancer Institute, National Institutes of Health, Rockville, MD, United States of America

E-mail: taceun.kwon@nih.gov**Keywords:** nuclear medicine, monte carlo radiation transport, computational human phantoms, organ absorbed doseSupplementary material for this article is available [online](#)**Abstract**

The exponential growth in the use of nuclear medicine procedures represents a general radiation safety concern and stresses the need to monitor exposure levels and radiation-related long term health effects in NM patients. In the current study, following our previous work on NCINM version 1 based on the UF/NCI hybrid phantom series, we calculated a comprehensive library of S values using the ICRP reference pediatric and adult voxel phantoms and established a library of biokinetic data from multiple ICRP Publications, which were then implemented into NCINM version 2. We calculated S values in two steps: calculation of specific absorbed fraction (SAF) using a Monte Carlo radiation transport code combined with the twelve ICRP pediatric and adult voxel phantoms for a number of combinations of source and target region pairs; derivation of S values from the SAFs using the ICRP nuclear decay data. We also adjusted the biokinetic data of 105 radiopharmaceuticals from multiple ICRP publications to match the anatomical description of the ICRP voxel phantoms. Finally, we integrated the ICRP phantom-based S values and adjusted biokinetic data into NCINM version 2. The ratios of cross-fire SAFs from NCINM 2 to NCINM 1 for the adult phantoms varied widely from 0.26 to 5.94 (mean = 1.24, IQR = 0.77–1.55) whereas the ratios for the pediatric phantoms ranged from 0.64 to 1.47 (mean = 1.01, IQR = 0.98–1.03). The ratios of absorbed dose coefficients from NCINM 2 over those from ICRP publications widely varied from 0.43 (colon for ^{99m}Tc -ECD) to 2.57 (active marrow for ^{99m}Tc -MAG3). NCINM 2.0 should be useful for dosimetrists and medical physicists to more accurately estimate organ doses for various nuclear medicine procedures.

Introduction

In diagnostic nuclear medicine (NM), medical benefits have been generally considered to outweigh radiation risks. With the advent of Single Photon Emission Computed Tomography (SPECT), Positron Emission Tomography (PET), and a surge of new radiopharmaceuticals, the number of NM procedures performed has increased in the last decades, especially in the United States (NCRP 2009, 2019). The emergence of theranostics in nuclear medicine (Yordanova *et al* 2017, Gomes Marin *et al* 2020), which combines diagnostics and therapy as a way to achieve a personalized treatment approach, also points towards an expansion of nuclear medicine for applications in medicine such as oncology, cardiology, neurology, and infectious and inflammatory

disorders. However, standard hybrid imaging technologies, combining SPECT or PET with Computed Tomography (CT), have raised concerns for patient radiation exposure (Brix *et al* 2014, Indrakanti *et al* 2022). Overall, the exponential growth in the use of NM procedures represents a general radiation safety concern and stresses the need to monitor exposure levels and radiation-related long term health effects in NM patients.

The calculation of radiation absorbed dose to organs and tissues in nuclear medicine commonly relies on the application of the Medical Internal Radiation Dose (MIRD) formalism (Loevinger *et al* 1991). The methods define the absorbed dose as the product of two factors: the time-integrated activity in a source organ, which represents the biokinetics of the radiopharmaceutical or radio-tracer, and organ dose conversion coefficients called S

values. S values can be directly computed from patient images by Monte Carlo radiation transport methods or pre-calculated using computational human phantoms, when a high level of precision is not required or patient images are not available. Model-based internal dosimetry software incorporates pre-computed S values into graphical user interfaces: OLINDA (Stabin and Farmer 2012), IDAC (Andersson *et al* 2017, 2014), and the National Cancer Institute dosimetry system for Nuclear Medicine (NCINM) (Villoing *et al* 2020). The anatomical accuracy of human anatomical models adopted for S value calculations has a substantial impact on the accuracy of organ doses in the calculators. In the comparison among the aforementioned three software, it was revealed that the absorbed dose coefficients could considerably vary depending on the adopted anatomical models with the ratio from 0.14 (OLINDA/NCINM) to 1.8 (IDAC/NCINM) (Villoing *et al* 2020).

In the past decades, computational human phantoms have been improved in terms of both flexibility and realism (Xu 2014), opening new perspectives for internal dosimetry. The non-uniform rational B-spline (NURBS)-based models, such as the series of pediatric and adult phantoms developed by the University of Florida and National Cancer Institute (Lee *et al* 2010), provides a greater anatomical realism and dosimetric accuracy compared to the mathematical equation-based stylized phantoms. More recently, the International Commission on Radiological Protection (ICRP) released a series of ten pediatric computational phantoms (ICRP 2020), which completes a full set of age-dependent phantoms with the ICRP adult reference phantoms (ICRP 2009). As interpatient anatomical variability is reported to have a substantial impact on absorbed doses in nuclear medicine, it is important to evaluate the impact of using different computational human phantoms on organ dosimetry in nuclear medicine. It is also crucial to derive dose coefficients by using the new international reference ICRP voxel phantom series.

In the current study, following our previous work on NCINM version 1 (Villoing *et al* 2020) based on the UF/NCI hybrid phantom series, we calculated a comprehensive library of S values using the ICRP reference pediatric and adult voxel phantoms and established a library of biokinetic data from multiple ICRP Publications. We implemented the new S values and the biokinetic data into a user-friendly software (NCINM version 2) which calculates absorbed dose coefficients and organ absorbed doses based on the patient parameters and administered activity.

Material and methods

We calculated S values in two steps using the MIRD formalism (Loevinger *et al* 1991): calculation of specific absorbed fraction (SAF) using a Monte Carlo radiation transport code combined with the twelve

ICRP pediatric and adult voxel phantoms for a number of combinations of source and target region pairs; derivation of S values from the SAFs using the nuclear decay data from ICRP Publication 107 (ICRP 2008a). We also adjusted the biokinetic data of 105 radiopharmaceuticals from multiple ICRP publications to match the anatomical description of the ICRP voxel phantoms. Finally, we integrated the ICRP phantom-based S values and adjusted biokinetic data into NCINM version 2.

ICRP voxel phantoms

We adopted the ICRP pediatric and adult voxel phantoms to calculate photon and electron SAFs. The ICRP pediatric voxel phantoms represent male and female newborn, 1-, 5-, 10-, and 15-year-old reference children. The phantoms have recently been published in ICRP Publication 143 (ICRP 2020) following the same definition of source and target organs and tissues as the adult male and female voxel phantoms published in ICRP Publication 110 (ICRP 2009). The binary voxel data of the pediatric phantoms, which can be directly read by MCNP6, were directly obtained from the electronic appendix of ICRP Publication 143. The lattice format files of the ICRP adult male and female phantoms were converted to binary voxel format. The matrix sizes of the pediatric and adult phantoms ranged from 7.2 (the adult male) to 55 (the pediatric phantoms) millions with the size of the voxel between 0.0003 (newborn) to 0.0365 (adult male) cm³. The material data libraries of the phantoms, including composition and density of each organ, and the tissue masses in skeletal regions, were also directly obtained from the electronic appendices of the ICRP publications.

Calculations of S values

The calculation of S values was conducted in three steps. First, photon and electron absorbed fractions (AFs), energy absorbed in target regions per energy emitted from source regions, were computed for 25 energy bins ranging from 10 keV to 6 MeV for each of the 12 pediatric and adult male and female voxel phantoms for 3,740 source-target pairs. Appendix A and B show the 68 source and 55 target regions, respectively, that were selected for the calculation of AFs. The energy (MeV) per source particle absorbed in target regions was scored by using *f8 tally where the secondary electron was tracked using a general-purpose Monte Carlo code, MCNP6 (Goorley *et al* 2016). Standard cross-section libraries available from MCNP6 were used with the default energy cutoffs for electron transport of 1 keV. A total of one billion particles were simulated for the energy below 1 MeV and 10 million particles were used for the energy above 1 MeV to reduce Monte Carlo statistical errors below 1% in most combinations of source and target regions. The whole Monte Carlo calculation of AFs took about a month using the Biowulf high-performance

computing servers available at the National Institutes of Health.

Second, we derived a library of SAFs, absorbed fractions divided by target region mass, combined with the twelve ICRP reference voxel phantoms. The target region masses for the pediatric and adult phantom series were obtained from ICRP Publication 143 and 110, respectively. For self-absorption SAFs, the absorbed fractions were divided by target region masses, combined with the mass of blood in each target region derived from the whole-body blood distribution of the pediatric (Wayson *et al* 2018) and adult (ICRP 2002) phantoms. Although the differences in the phantom organ mass (i.e. parenchyma mass, exclusive of blood) and the reference blood-inclusive target mass can result in differences in the self-absorption fraction for photons, the absolute differences in the SAFs would be minor (ICRP 2016). For cross-fire SAFs, the target region masses calculated from the phantoms were directly used according to the principle adopted in the ICRP Publication 133 (ICRP 2016) that the SAF is independent of target mass. We adopted the SAFs for the left colon wall, right colon wall, rectosigmoid colon wall, esophagus wall, small intestine wall, and stomach wall of the adult male and female voxel phantoms from ICRP Publication 133 (ICRP 2016), which are based on the mathematical models describing the thin radiosensitive layers (ICRP 2006). For source regions of bone marrow, trabecular bone, and cortical bone, the SAFs from ICRP Publication 133, which were calculated using the micro-CT imaging data of spongiosa, were also directly applied to the S value calculation. We adopted the skeletal dose response functions (ICRP 2010) to calculate SAFs for target regions of active marrow and endosteum. The f4 tally was used to score fluence in the skeletal trabecular regions by 25 bone sites. Two sets of dose response functions, one for active marrow and the other for endosteum, were then multiplied to the fluences to obtain absorbed dose (Gy) to active marrow and endosteum, which were then converted to absorbed energy per target tissue mass ($\text{MeV}/\text{kg}^{-1}$). SAFs (kg^{-1}) were derived by dividing the results by the energy emitted from source regions. To evaluate the impact of the computational phantom series on SAFs, we compared the SAFs calculated from the ICRP voxel phantoms with those from the UF/NCI phantoms. To investigate the impact of different phantom libraries on SAFs, we compared the SAFs between the UF/NCI phantoms (previously published) and the ICRP reference phantoms.

Finally, we created an in-house MATLAB script to derive S values from the photon and electron SAFs by adopting the energy spectrum of 299 radionuclides available in ICRP Publication 107 (ICRP 2008a), which are available for diagnostic and therapeutic nuclear medicine procedures. Photon spectrum included gamma rays (prompt and delayed), x-rays, annihilation photons, and electron spectrum included beta

+ and beta- particles, internal conversion electrons, and Auger electrons. Linear interpolation was used to derive SAF values for a specific photon or electron energy from the monoenergy-based SAFs calculated in the previous step. The resulting S value matrix was a function of 299 radionuclides, 55 target regions, 68 source regions, and 12 phantoms.

ICRP biokinetic data

We collected biokinetic data for 105 radiopharmaceuticals summarized in the ICRP publications 53 (ICRP 1998a), 80 (ICRP 1998b) or 106 (ICRP 2008b), corresponding to 15 different radionuclides. The list of radiopharmaceuticals, corresponding radionuclides, and their reference are listed in appendix C.

In order to simplify both the implementation in the software and its usability, we defined separately the various modes of administration (intravenous, oral) and specific features related to the radiopharmaceutical (uptake, blocking agent or not). For example, we included the biokinetic data of $^{99\text{m}}\text{Tc}$ -pertechnetate in the three different categories:

- $^{99\text{m}}\text{Tc}$ -pertechnetate (intravenous, no blocking agent)
- $^{99\text{m}}\text{Tc}$ -pertechnetate (intravenous, blocking agent)
- $^{99\text{m}}\text{Tc}$ -pertechnetate (oral, no blocking agent)

We also discriminated the various health conditions that influenced the biodistribution of a radiopharmaceutical. For example, we collected the biokinetic data of ^{123}I -sodium iodo hippurate in the four different health conditions:

- ^{123}I -sodium iodo hippurate (normal renal function)
- ^{123}I -sodium iodo hippurate (abnormal renal function)
- ^{123}I -sodium iodo hippurate (left kidney blockage)
- ^{123}I -sodium iodo hippurate (right kidney blockage)

While we translated the ICRP biokinetic data to the organs and tissues of the ICRP voxel phantoms, we observed differences in the definition of source regions and we modified the ICRP biokinetic data to match the ICRP voxel phantoms so we conducted three key modifications to the ICRP biokinetic data. First, the biokinetic data are provided in ICRP Publications for upper large intestine (ULI) and lower large intestine (LLI) following the geometric definition of the large intestines in the stylized phantoms, whereas the large intestines in the ICRP voxel phantoms are separated into the left colon (LC), right colon (RC), and rectosigmoid colon (RS). We adopted the conversion method reported by Andersson *et al.* (Andersson *et al* 2014) as following:

$$\sigma_{RC} = 0.71 \times \sigma_{ULI} \quad (1)$$

$$\sigma_{LC} = 0.29 \times \sigma_{ULI} + 0.56\sigma_{LLI} \quad (2)$$

$$\sigma_{RS} = 0.44 \times \sigma_{LLI} \quad (3)$$

where σ_{RC} , σ_{LC} , σ_{RS} , σ_{ULI} , and σ_{LLI} are the time-integrated activity coefficients (TIACs, in hours) of the RC, LC, RS, ULI and LLI, respectively. Second, the ICRP Publications report the TIACs in whole organs for the walled organs such as the gallbladder, heart, small intestine, stomach and urinary bladder. These organs are separated into the wall and contents in the ICRP voxel phantoms. We weighted the TIACs of these walled organs by using the masses of the wall and contents in the ICRP phantoms to obtain the TIACs in the wall and content, separately, using the following equations.

$$\sigma_{wall} = \frac{m_{wall}}{m_{wall} + m_{cont}} \times \sigma_{total} \quad (4)$$

$$\sigma_{cont} = \frac{m_{cont}}{m_{wall} + m_{cont}} \times \sigma_{total} \quad (5)$$

where σ_{wall} , $\sigma_{content}$, and σ_{total} are the TIACs of the organ wall, the organ content, and the whole organ, respectively, and m_{wall} and m_{cont} are the masses of the organ wall and the organ content. As organ masses vary with age and gender, different weighting factors were used (Appendix D). Note that for the urinary bladder, one of the walled organs, we assigned the TIACs exclusively to the urinary bladder contents. In all cases where ICRP considered the urinary bladder a separate entry in the biokinetic data, the urinary bladder as a source region represents the bladder contents (i.e. urine) rather than the entire bladder. Third, ICRP Publication 53 provides the TIACs for the source definitions ‘other organs and tissues’ or ‘total body’ depending on different radiopharmaceuticals. We assigned the TIACs for ‘other organs and tissues’ to the remaining tissues (all tissues minus the selected source regions) without adjustment. However, the TIACs for ‘total body’ had to be modified by subtracting the TIACs to all other sources organs, using the following formula:

$$\sigma_{remaining\ tissues} = \sigma_{total\ body} - \sum_i \sigma_{source\ i} \quad (6)$$

where $\sigma_{remaining\ tissues}$, $\sigma_{total\ body}$, and $\sigma_{source\ i}$ are the TIACs in the remaining tissues that we defined in our calculations, the total body that is defined in the ICRP biokinetic data, and source region i .

Absorbed dose coefficients

The libraries of S values and biokinetic data were implemented into the graphical user interface-based dose calculator, NCINM. The user interface of NCINM version 1.0 was improved for users to select one of the two phantom libraries (UF/NCI and ICRP) for extracting S values and the radiopharmaceutical for biokinetic data. The software was coded and compiled into execution files using multi-platform language, Xojo (Xojo, Inc. Austin, TX).

We computed absorbed doses per unit administered activity (mGy/MBq), also called absorbed dose coefficients, for four illustrative radiopharmaceuticals that are commonly used in nuclear medicine procedures: ^{111}In -DTPA-octreotide, ^{99m}Tc -MAG3, ^{99m}Tc -ECD, and ^{18}F -FDG. For validation purposes, we compared the absorbed dose coefficients for adult male and female calculated from NCINM version 2 with those from IDAC 2.1 (Andersson *et al* 2017), dosimetry software which uses the SAFs based on the ICRP adult voxel phantoms, for five major organs with a tissue weighting factor of 0.12 (i.e. red bone marrow, breast, colon, lungs, and stomach). The absorbed dose coefficients were also compared with those from NCINM version 1 (UF/NCI phantoms) and ICRP publications (stylized phantoms).

Results

SAF and S values

A library of SAFs was calculated using the twelve ICRP pediatric and adult voxel phantoms for 25 energies, 68 source regions, and 55 target regions. Photon and electron self-absorption SAFs did not show significant differences between the UF/NCI phantoms and the ICRP phantoms (figure 1(A)). Ratios of the self-absorption SAFs calculated from the ICRP phantoms to those from the UF/NCI phantoms ranged from 0.81 to 1.11 (interquartile range = 0.99–1.01; mean = 1.00; median = 1.00) across 12 pediatric and adult phantoms. The greatest difference was observed in the SAF for the prostate of the 5-year-old male phantom. For adult phantoms, the differences in the self-absorption SAFs were relatively greater than those for pediatric phantoms; however, most differences were less than 5% with a interquartile range of 0.97–1.02.

Relatively greater differences were observed in crossfire photon SAFs comparisons (figure 1(B)). The SAF ratios (ICRP over UF/NCI) ranged from 0.26 to 5.94 (interquartile range = 0.97–1.03; mean = 1.05; median = 1.00) across 12 pediatric and adult phantoms. The smallest and largest ratios were observed in SAF(spleen←pancreas) for the adult female phantom and SAF(thyroid←esophagus) for the adult male phantom, respectively. Compared to the self-absorption SAFs, the differences in the SAF ratios depending on pediatric phantoms and adult phantoms were much more substantial. The ratios for the adult phantoms varied widely from 0.26 to 5.94 (interquartile range = 0.77–1.55; mean = 1.24; median = 1.03) whereas the ratios for the pediatric phantoms ranged from 0.64 to 1.47 (interquartile range = 0.98–1.03; mean = 1.01; median = 1.00). The median of the ratio was close to unity in most phantoms, except for the adult male phantom with the median of 1.15.

A library of S values was created for 299 radionuclides, 12 pediatric and adult phantoms, 68 source, and 55 target regions. The S values were integrated into

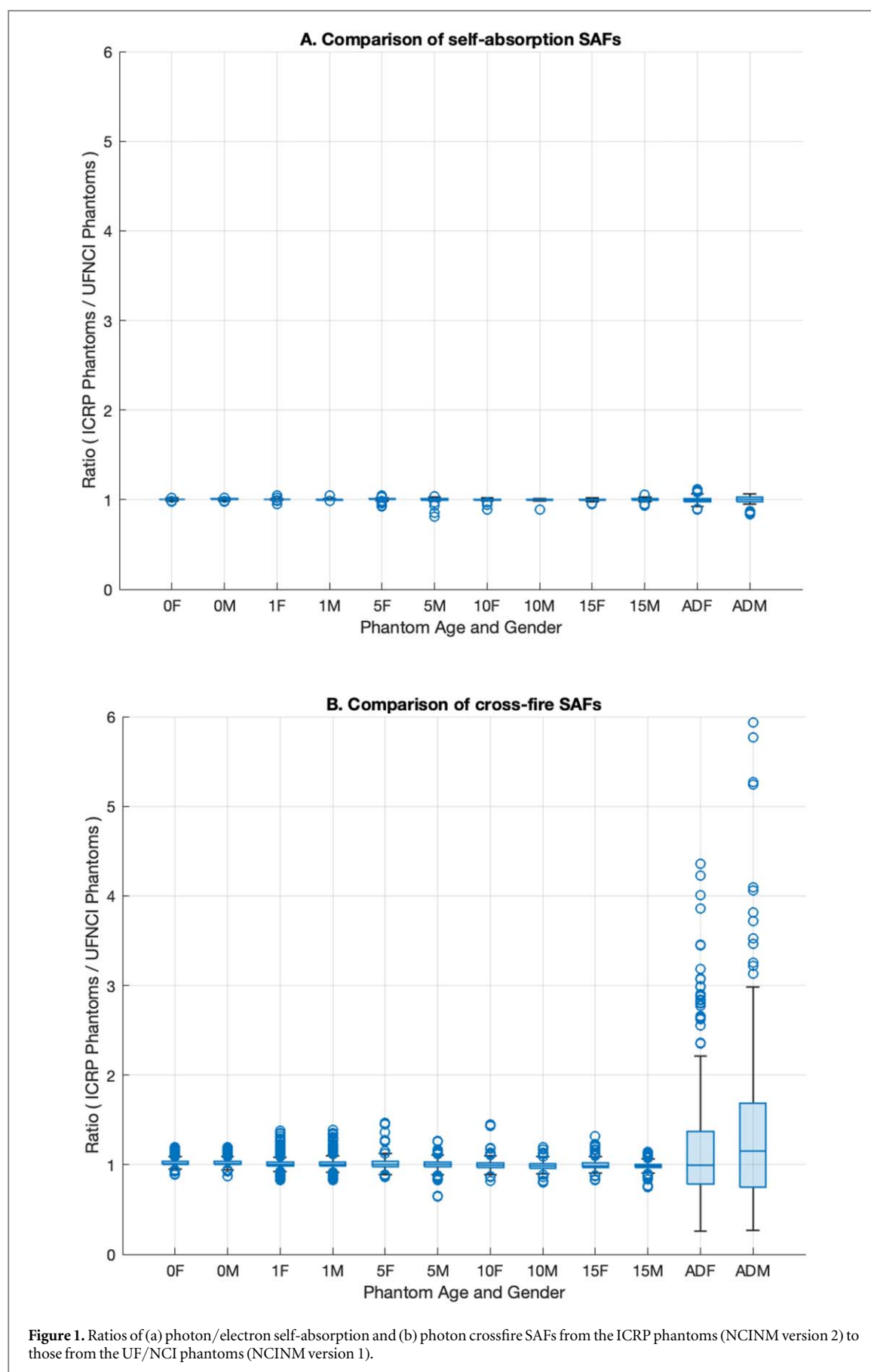


Figure 1. Ratios of (a) photon/electron self-absorption and (b) photon crossfire SAFs from the ICRP phantoms (NCINM version 2) to those from the UF/NCI phantoms (NCINM version 1).

NCINM version 2 to derive absorbed dose coefficients as per user input data. When external dose calculations are desired, S values can be exported into ASCII files through

the NCINM user interface with the user input of a radionuclide, phantom, and source regions. Illustrative S values for six selected radionuclides (^{68}Ga , ^{123}I , ^{131}I , ^{111}In ,

Table 1. Comparison of Time-Integrated Activity Coefficients (TIACs) for ^{75}Se -HCAT between ICRP Publication 53 and NCINM2.

ICRP Publication 53		NCINM 2	
Source region	TIAC (h)	Source region	TIAC (h)
Total body (excluding contents of GI tract)	131.04	Remaining tissue	95.86
Gallbladder	27.36	Gallbladder contents	23.3365
		Gallbladder wall	4.0235
Liver	7.82	Liver	7.82
Stomach contents	1	Stomach contents	1
Small intestine contents	58.08	Small intestine contents	58.08
Upper large intestine contents	12.7	Colon left contents	16.731
Lower large intestine contents	23.3	Colon right contents	9.017
		Colon rectosigmoid contents	10.252

^{177}Lu , and $^{99\text{m}}\text{Tc}$) are provided in the electronic supplementary data.

Biokinetic model

A library of biokinetic data (i.e. Time-Integrated Activity Coefficients, previously named residence times) was created for 15 radionuclides and 105 radiopharmaceuticals by extracting raw data from multiple ICRP Publications and modifying them to match the definition of source and target regions in the ICRP voxel phantoms. The full dataset is provided in the electronic supplementary data. Table 1 shows an example TIAC in the case of ^{75}Se -HCAT from ICRP Publication 53 and those modified for NCINM version 2. The TIAC for the gallbladder in ICRP Publication 53 was divided into those for gallbladder contents and wall (equations (4) and (5)), and that for the upper and lower large intestine in ICRP Publication 53 were adjusted to left, right, and rectosigmoid colon (equations (1), (2), and (3)). In addition, instead of the TIAC for the total body in ICRP Publication 53, the remaining TIAC other than the gallbladder contents, the gallbladder wall, and the liver was assigned to the remaining tissue (equation (6)).

Absorbed dose coefficients

Absorbed dose coefficients (mGy/MBq) are automatically calculated and used for organ dose calculations within the NCINM version 2. For illustrative purposes, we computed the absorbed dose coefficients for four common radiopharmaceuticals (^{111}In -DTPA-octreotide, $^{99\text{m}}\text{Tc}$ -MAG3, $^{99\text{m}}\text{Tc}$ -ECD, ^{18}F -FDG) for 55 target organs and 12 pediatric and adult phantoms, which were tabulated in the electronic supplementary data.

The absorbed dose coefficients from NCINM 2 were comparable with those from IDAC 2.1. Although differences more than 10% were observed in a few absorbed dose coefficients for breast and lungs, most ratios of the absorbed dose coefficients (NCINM 2 over IDAC 2.1) were within a narrow range from 0.96 to 1.08.

The differences in the absorbed dose coefficients between NCINM2 and NCINM1 or ICRP data varied depending on radiopharmaceuticals and organs

(table 2). The ratio of the absorbed dose coefficients from NCINM 2 to those from NCINM 1 ranged from 0.70 to 1.47 across the four radiopharmaceuticals and the five organs, and both the smallest and largest ratios were observed in the dose coefficients for stomach. However, for active marrow, one of the most radio-sensitive organs, the differences in the dose coefficients, except for ^{18}F -FDG for the adult female, were less than 17% with the ratio ranging from 0.98 to 1.17. The range of the ratio for breast, colon, and lungs was from 0.8 to 1.10, from 0.78 to 1.15, and from 0.99 to 1.38, respectively.

Much greater differences were observed in the comparison between NCINM 2 and the ICRP dose coefficients. The ratio widely varied from 0.43 to 2.57 across the four radiopharmaceuticals and the five organs. The smallest and largest ratios were observed in the dose coefficient for colon for $^{99\text{m}}\text{Tc}$ -ECD (0.43) and for active marrow for $^{99\text{m}}\text{Tc}$ -MAG3 (2.57), respectively. Although the ratio varied depending on radiopharmaceuticals and organs, the dose coefficients for active marrow of NCINM 2 were noticeably greater than those from ICRP publications regardless of radiopharmaceuticals with the ratio ranging from 1.12 to 2.57. In addition, for the breast, the dose coefficients of NCINM 2.0 were also significantly greater for all radiopharmaceuticals except $^{99\text{m}}\text{Tc}$ -MAG3.

NCINM 2

Figure 2 shows the graphical user interface of the NCINM 2, where the comprehensive libraries of S value and biokinetic data were embedded. Compared to NCINM 1, new features to select the phantom libraries (UF/NCI phantoms versus ICRP phantoms) (left panel and top) and radiopharmaceuticals (left panel and bottom) were created. When TIACs for a given radiopharmaceutical are available, users can select a phantom library and radionuclide, and then enter TIACs in source regions to calculate organ doses. When TIACs are not available, users can select the phantom library and radiopharmaceutical and the TIACs in the source regions (middle panel) are automatically populated with the ICRP biokinetic



Figure 2. Graphical user interface of NCINM 2 where organ doses are calculated for the ICRP adult male voxel phantom when 3700 MBq of ^{18}F -FDG is administered.

data. Absorbed doses to the target regions and effective dose are calculated and displayed in the right panel.

Discussion

Our study has the following strengths. First, we derived S values from the ICRP pediatric reference voxel phantoms for the first time. The S value library and corresponding absorbed dose coefficients should be useful reference data to calculate organ and effective doses for patients undergoing nuclear medicine procedures. Second, a comprehensive library of biokinetic data for more than 100 radiopharmaceuticals was established following the definition of source regions of the new ICRP pediatric and adult voxel phantoms. The data can be also applied to the S values derived from other modern voxel or hybrid phantom libraries where the definition of source regions may be different from that of the old stylized phantoms. Third, the library of S values and biokinetic data were combined into a user-friendly computer program allowing for rapid calculations of organ and effective doses even when dosimetry calculations are sought for many patients.

We performed comparisons of SAFs between the UF/NCI and ICRP voxel phantoms (figure 1). The noticeable differences in SAFs were mainly observed between the UF/NCI and ICRP adult phantoms but not between the UF/NCI and ICRP pediatric phantoms. This can be explained by the larger anatomical variability between the two types of adult phantoms than between the two pediatric phantom libraries. Note that ICRP pediatric phantoms were developed by

minor adjustments to the UF/NCI pediatric phantoms (ICRP 2020). The differences in the SAFs between the two types of the adult phantoms were more substantial in the crossfire SAFs (figure 1(b)) than in the self-absorption SAFs (figure 1(a)). This is due to the fact that the UF/NCI and ICRP adult phantoms have anatomical variability but were developed based on the same ICRP reference organ mass data (ICRP 2002). Since the self-absorption AFs of photon and electron are barely affected by organ geometry at a given volume, the self-absorption SAF essentially depends on the organ mass. On the contrary, the crossfire energy transfer, mainly achieved by photons, is heavily affected by a distance between source and target organs. As the distance between source and target organs is longer, average flight lengths of photons are longer and intensity of photons departing toward the target organ decreases. Therefore, the large differences in the crossfire SAFs can be explained by the differences in the source-to-target organ distances between the UF/NCI and ICRP phantom libraries.

In the current study, S value comparisons were not performed because S values have dosimetric significance only when source and target regions are specified considering radiopharmaceutical's biokinetics. Instead, the practical impact of the inter-phantom anatomical variability on the radiopharmaceutical dosimetry was assessed by the absorbed dose coefficient comparisons.

A good agreement was observed in the comparison of absorbed dose coefficients between NCINM 2 and IDAC 2.1, supporting the overall validity of the S values and the calculation algorithm in NCINM 2. It is

Table 2. Comparison of absorbed dose coefficients for four radiopharmaceuticals calculated for the adult male (AM) and female (AF) phantoms between NCINM2 (ICRP phantoms) and IDAC 2.1 (ICRP phantoms), between NCINM2 (ICRP phantoms) and NCINM1 (UF/NCI phantoms), and between NCINM2 (ICRP phantoms) and ICRP Publications (stylized phantoms).

Organs	Ratio	¹¹¹ In-DTPA-octreotide		^{99m} Tc-MAG3		^{99m} Tc-ECD		¹⁸ F-FDG	
		AM	AF	AM	AF	AM	AF	AM	AF
Breast	NCINM2/IDAC 2.1	0.98	1.13	0.99	1.12	0.96	1.08	1.04	1.12
	NCINM2/NCINM1	0.95	1.01	0.80	0.89	1.02	0.94	0.96	1.10
	NCINM2/ICRP ^a	1.39	1.73	1.00	1.36	1.32	1.51	1.04	1.45
Colon	NCINM2/IDAC 2.1	1.00	1.00	0.92	0.96	0.97	0.97	1.02	1.01
	NCINM2/NCINM1	1.08	0.85	0.81	1.15	0.78	0.80	0.97	0.79
	NCINM2/ICRP ^a	1.40	1.23	0.94	1.50	0.43	0.52	0.84	1.04
Lungs	NCINM2/IDAC 2.1	1.11	1.12	1.04	1.03	0.96	0.96	0.96	0.94
	NCINM2/NCINM1	1.38	1.26	1.03	0.99	1.18	1.02	1.07	1.05
	NCINM2/ICRP ^a	1.42	1.51	0.99	1.08	1.03	1.10	0.90	1.12
Stomach	NCINM2/IDAC 2.1	1.01	1.01	1.00	1.00	0.98	0.99	1.06	1.06
	NCINM2/NCINM1	0.93	1.37	0.70	1.07	1.47	1.19	1.11	0.95
	NCINM2/ICRP ^a	1.38	2.28	0.82	1.13	1.73	1.53	1.04	1.13
Active marrow	NCINM2/IDAC 2.1	1.04	1.04	1.04	1.04	1.01	1.01	0.97	0.98
	NCINM2/NCINM1	1.00	1.17	0.98	1.03	1.02	1.15	1.01	1.31
	NCINM2/ICRP ^a	1.40	1.67	2.57	2.42	1.29	1.57	1.12	1.27

^a ICRP dose coefficients for ¹¹¹In-DTPA-octreotide, ^{99m}Tc-MAG3, ^{99m}Tc-ECD, and ¹⁸F-FDG were taken from ICRP Publication 106, 80, 106, and 106, respectively.

plausible that the small differences between the two software arose from the differences in the Monte Carlo code used for the S value calculation.

The differences in the SAFs between the UF/NCI and ICRP phantom libraries directly led to the differences in the dose coefficients between NCINM 2 and NCINM 1. In particular, for organs to which the radiopharmaceuticals are not directly absorbed, the difference in the crossfire SAFs resulted in the significant differences in the dose coefficients. Therefore, the dose coefficients for the stomach for ^{99m}Tc-ECD greater than those from NCINM 1 (1.73 and 1.53 times for male and female, respectively) can be explained by the larger SAFs resulting from the shorter source-to-target organ distances in the ICRP reference phantoms than in the UF/NCI phantoms. Greater differences were observed in the dose coefficient comparisons between NCINM 2 and ICRP publications. These differences arose from the large anatomical variability between the ICRP voxel phantoms used in NCINM 2 and the stylized phantoms used in the calculation of the ICRP dose coefficients. The stylized phantoms were not only geometrically oversimplified but also based on an old anatomical data in ICRP Publication 23. These differences in the dose coefficients are practically important because the ICRP data are currently used in the fields of nuclear medicine and radiation protection. In particular, the dose coefficients for the active marrow of NCINM 2 were greater than those of the ICRP data by up to 2.57 times (table 2), indicating that the use of the ICRP reference dose coefficients can considerably underestimate the actual dose to the active marrow. Thus, the use of the

more accurate dose coefficients of NCINM 2 may lead to lower administration dosages of radiopharmaceuticals to avoid the potential active marrow toxicity.

We are aware of the following limitations of our tool. First, the S values were calculated from the ICRP pediatric and adult phantoms representing reference body sizes. The data may not be applicable to patients with non-reference height or weight. The amount of inter-organ fat should be different between thin and obese patients which may affect crossfire S values. Further simulation and analysis using patient data with various body sizes is required to better understand the impact of body size on internal exposure dosimetry. Second, we are aware that some updates have been applied to the biokinetic models in the ICRP Publication 128. We plan to implement these updates in NCINM.

Conclusion

We first calculated a comprehensive library of S values from the ICRP reference pediatric voxel phantoms that were recently released. We also compiled a library of biokinetic models corresponding to the definition of source regions in the ICRP voxel phantoms from several ICRP publications. The resulting S values and biokinetic models were implemented into a user-friendly computer program, NCINM version 2, which follows the previous version 1 which was only based on the UF/NCI pediatric and adult voxel phantoms. NCINM 2.0 should be useful for dosimetrists and

medical physicists to more accurately estimate organ doses for various nuclear medicine procedures. NCINM 2 is available at no cost through <http://ncidose.cancer.gov>.

Acknowledgments

This research was funded by the intramural research program of the National Institutes of Health (NIH), National Cancer Institute, Division of Cancer Epidemiology and Genetics. This work utilized the computational resources of the NIH High-Performance Computing Biowulf cluster (<http://biowulf.nih.gov>).

Data availability statement

All data that support the findings of this study are included within the article (and any supplementary files).

Appendix A.

List of 68 source regions considered in the calculation of specific absorbed fractions (L = Left, R = Right, LR = Left and Right, ET = Extrathoracic, LN = Lymph nodes, RECT = Rectosigmoid).

Table A1.

1	Adipose	21	Esophagus	41	Lymph Nodes ET	61	Thyroid
2	Adrenal L	22	ET2	42	LN but ET/Thoracic	62	Tongue
3	Adrenal R	23	Gallbladder Content	43	LN Thoracic	63	Tonsils
4	Adrenal LR	24	Gallbladder Wall	44	Muscle	64	Trabecular Bone Marrow ^c
5	Blood Body	25	Gonads	45	Nasal Anterior	65	Trabecular Bone Mineral ^d
6	Blood Heart	26	Heart Wall	46	Nasal Posterior	66	Ureters
7	Blood Body + Heart	27	Kidney L	47	Oral Cavity	67	Urinary Bladder Content
8	Brain	28	Kidney L Cortex	48	Pancreas	68	Urinary Bladder Wall
9	Breast	29	Kidney L Medulla	49	Pituitary Gland		
10	Breast Adipose	30	Kidney L Pelvis	50	Prostate or Uterus		
11	Breast Glandular	31	Kidney R	51	Salivary Glands		
12	Bronchi	32	Kidney R Cortex	52	Skin		
13	Colon L Content	33	Kidney R Medulla	53	Small Intestine Content		
14	Colon L Wall	34	Kidney R Pelvis	54	Small Intestine Wall		
15	Colon R Content	35	Kidney LR	55	Spinal Cord		
16	Colon R Wall	36	Lenses of Eye	56	Spleen		
17	Colon RECT Content	37	Liver	57	Stomach Content		
18	Colon RECT Wall	38	Lung L	58	Stomach Wall		
19	Cortical Bone Marrow ^a	39	Lung R	59	Teeth		
20	Cortical Bone Mineral ^b	40	Lung LR	60	Thymus		

^a Cortical bone marrow: The marrow contained in the medullary cavities in the shafts of the long bones.

^b Cortical bone mineral: The mineral contained in the cortical regions of all bones.

^c Trabecular bone marrow: The marrow contained in the spongiosa regions of all bones (marrow fraction of spongiosa bones).

^d Trabecular bone mineral: The mineral in the spongiosa regions of all bones (mineral bone fraction of spongiosa bones).

Appendix B.

List of 55 target regions considered in the calculation of specific absorbed fractions (RECT = Recto-sigmoid, L = Left, R = Right, ET = Extrathoracic, LN = Lymph nodes, RECT = Rectosigmoid).

1	Adipose	21	Kidney Cortex L	41	Prostate or Uterus
2	Adrenal	22	Kidney cortex R	42	Salivary Glands
3	Adrenal L	23	Kidney Medulla L	43	Skin
4	Adrenal R	24	Kidney Medulla R	44	Small Intestine Wall
5	Bronchi	25	Kidney Pelvis L	45	Spinal Cord
6	Brain	26	Kidney Pelvis R	46	Spleen
7	Breast Adipose	27	Lenses of Eye	47	Stomach Wall
8	Breast Glandular	28	Liver	48	Thymus
9	Colon Wall	29	Lung	49	Thyroid
10	Colon	30	Lung L	50	Tongue
	RECT Wall				
11	Colon Wall L	31	Lung R	51	Tonsils
12	Colon Wall R	32	LN ET	52	Ureters
13	Esophagus	33	LN but ET/ Thoracic	53	Urinary Bladder Wall
14	ET Region	34	LN Thoracic	54	Active Marrow
15	Gallbladder Wall	35	Muscle	55	Shallow Marrow
16	Gonads	36	Nasal Anterior		
17	Heart Wall	37	Nasal Posterior		
18	Kidney	38	Oral Mucosa		
19	Kidney R	39	Pancreas		
20	Kidney L	40	Pituitary Gland		

Appendix C.

List of radiopharmaceuticals for which biokinetic models were collected from the ICRP Publications 53, 80, and 106.

Radionuclide	Radiopharmaceutical	ICRP	Specification	Denomination in NCINM
^3H	^3H neutral fat and free fatty acids	80	—	^3H -neutral fat, free fatty acids (ICRP 80)
^{11}C	^{11}C -acetate	106	—	^{11}C -acetate (ICRP 106)
	^{11}C -amino acids	106	Generic model	^{11}C -amino acids (generic model) (ICRP 106)
	^{11}C -brain receptor substances	106	Generic model	^{11}C -brain receptor substances (generic model) (ICRP 106)
	^{11}C -methionine	106	L-[methyl- ^{11}C]-methionine	^{11}C -methionine (ICRP 106)
	^{11}C -thymidine	80	[methyl- ^{11}C] [2- ^{11}C]	^{11}C -thymidine ([Methyl- ^{11}C]) (ICRP 80) ^{11}C -thymidine ([2- ^{11}C]) (ICRP 80)
	^{11}C substances	106	Realistic maximum	^{11}C (realistic maximum model) (ICRP 106)
^{14}C	^{14}C neutral fat and free fatty acids	80	—	^{14}C -neutral fat, free fatty acids (ICRP 80)
	^{14}C -urea	80	Normal case, oral administration	^{14}C -urea (normal case, oral administration) (ICRP 80)
			Normal case, CO_2 -pool	^{14}C -urea (normal case, CO_2 -pool) (ICRP 80)
			Helicobacter positive patient, oral administration	^{14}C -urea (helicobacter positive patient, oral administration) (ICRP 80)
			Helicobacter positive patient, CO_2 -pool	^{14}C -urea (helicobacter positive patient, CO_2 -pool) (ICRP 80)
^{15}O	^{15}O -water	106	—	^{15}O -water (ICRP 106)
^{18}F	^{18}F -amino acids	106	—	^{18}F -amino acids (generic model) (ICRP 106)
	^{18}F -brain receptor substances	106	Generic model	^{18}F -brain receptor substances (generic model) (ICRP 106)
	^{18}F -FDG	106	—	^{18}F -FDG (ICRP 106)
	^{18}F -L-dopa	106	—	^{18}F -L-dopa (ICRP 106)
^{51}Cr	^{51}Cr -EDTA	53	Intravenous, normal renal function	^{51}Cr -EDTA (intravenous, normal renal function) (ICRP 53)

(Continued.)

			Intravenous, abnormal renal function	51Cr-EDTA (intravenous, abnormal renal function) (ICRP 53)
			Oral	51Cr-EDTA (oral) (ICRP 53)
⁶⁷ Ga	⁶⁷ Ga-citrate	53	—	⁶⁷ Ga-citrate (ICRP 53)
⁶⁸ Ga	⁶⁸ Ga-EDTA	80	—	⁶⁸ Ga-EDTA (ICRP 80)
⁷⁵ Se	⁷⁵ Se-amino acids	106	—	⁷⁵ Se-amino acids (ICRP 106)
	⁷⁵ Se-HCAT	53	—	⁷⁵ Se-HCAT (ICRP 53)
^{99m} Tc	^{99m} Tc-apcitide	106	—	^{99m} Tc-apcitide (ICRP 106)
	^{99m} Tc-EC	106	Normal renal function	^{99m} Tc-EC (Normal renal function) (ICRP 106)
			Abnormal renal function	^{99m} Tc-EC (Abnormal renal function) (ICRP 106)
	^{99m} Tc-ECD	106	—	^{99m} Tc-ECD (ICRP 106)
	^{99m} Tc-furifosmin	106	Resting subject	^{99m} Tc-furifosmin (resting subject) (ICRP 106)
			Exercise	^{99m} Tc-furifosmin (exercise) (ICRP 106)
	^{99m} Tc-HIG	80	—	^{99m} Tc-HIG (ICRP 80)
	^{99m} Tc-HM-PAO	80	—	^{99m} Tc-HM-PAO (ICRP 80)
	^{99m} Tc-IDA derivatives	53	Normal hepato-biliary conditions	^{99m} Tc-IDA derivatives (normal hepato-biliary conditions) (ICRP 53)
			Parenchymal liver disease	^{99m} Tc-IDA derivatives (parenchymal liver disease) (ICRP 53)
			Occlusion of the cystic duct	^{99m} Tc-IDA derivatives (occlusion of the cystic duct) (ICRP 53)
			Occlusion of the common bile duct	^{99m} Tc-IDA derivatives (occlusion of the common bile duct) (ICRP 53)
	^{99m} Tc-MAA	53	—	^{99m} Tc-MAA (ICRP 53)
	^{99m} Tc-MAG3	80	Normal renal function	^{99m} Tc-MAG3 (normal renal function) (ICRP 80)
			Abnormal renal function	^{99m} Tc-MAG3 (abnormal renal function) (ICRP 80)
	^{99m} Tc-markers, non-absorbable	53	Oral administration of fluids	^{99m} Tc-markers, non-absorbable (oral administration of fluids) (ICRP 53)
			Oral administration of solids	^{99m} Tc-markers, non-absorbable (oral administration of solids) (ICRP 53)
	^{99m} Tc-MIBI	80	Resting subject	^{99m} Tc-MIBI (resting subject) (ICRP 80)
			Exercise	^{99m} Tc-MIBI (exercise) (ICRP 80)
	^{99m} Tc-labelled small colloids	106	Time to removal: 6 h	^{99m} Tc-labelled small colloids (time to removal: 6 h) (ICRP 106)
			Time to removal: 18 h	^{99m} Tc-labelled small colloids (time to removal: 18 h) (ICRP 106)
¹¹¹ In	^{99m} Tc-monoclonal antibodies	106	Intact antibody	^{99m} Tc-monoclonal antibodies (intact antibody) (ICRP 106)
			F(ab') ₂ fragments	^{99m} Tc-monoclonal antibodies (F(ab') ₂ fragments) (ICRP 106)
			F(ab') fragments	^{99m} Tc-monoclonal antibodies (F(ab') fragments) (ICRP 106)
	^{99m} Tc-pertechnegas	80	—	^{99m} Tc-pertechnegas (ICRP 80)
	^{99m} Tc-pertechnetate	53	Intravenous, no blocking agent	^{99m} Tc-pertechnetate (intravenous, no blocking agent) (ICRP 53)
			Intravenous, blocking agent	^{99m} Tc-pertechnetate (intravenous, blocking agent) (ICRP 53)
			Oral, no blocking agent	^{99m} Tc-pertechnetate (oral, no blocking agent) (ICRP 53)
	^{99m} Tc-RBC	53	—	^{99m} Tc-RBC (ICRP 53)
	^{99m} Tc-Technegas	80	—	^{99m} Tc-Technegas (ICRP 80)
	^{99m} Tc-tetrofosmin	106	Resting subject	^{99m} Tc-tetrofosmin (resting subject) (ICRP 106)
¹¹¹ In	^{99m} Tc-furifosmin	106	Exercise	^{99m} Tc-furifosmin (exercise) (ICRP 106)
	^{99m} Tc-WBC	53	—	^{99m} Tc-WBC (ICRP 53)
	¹¹¹ In-HIG	80	—	¹¹¹ In-HIG (ICRP 80)
	¹¹¹ In-monoclonal antibodies	106	Intact antibody	¹¹¹ In-monoclonal antibodies (intact antibody) (ICRP 106)
			F(ab') ₂ fragments	¹¹¹ In-monoclonal antibodies (F(ab') ₂ fragments) (ICRP 106)
¹²³ I			F(ab') fragments	¹¹¹ In-monoclonal antibodies (F(ab') fragments) (ICRP 106)
	¹¹¹ In-octreotide	106	—	¹¹¹ In-octreotide (ICRP 106)
	¹²³ I-iodide	53	Thyroid blocked, uptake 0%	¹²³ I-iodide (thyroid blocked, uptake 0%) (ICRP 53)

(Continued.)

			Thyroid uptake 5%	123I-iodide (thyroid uptake 5%) (ICRP 53)
			Thyroid uptake 15%	123I-iodide (thyroid uptake 15%) (ICRP 53)
			Thyroid uptake 25%	123I-iodide (thyroid uptake 25%) (ICRP 53)
			Thyroid uptake 35%	123I-iodide (thyroid uptake 35%) (ICRP 53)
			Thyroid uptake 45%	123I-iodide (thyroid uptake 45%) (ICRP 53)
			Thyroid uptake 55%	123I-iodide (thyroid uptake 55%) (ICRP 53)
	¹²³ I-BMIPP	106	—	123I-BMIPP (ICRP 106)
	¹²³ I-IPPA	106	—	123I-IPPA (ICRP 106)
	¹²³ I-brain receptor substances	106	Generic model	123I-brain receptor substances (generic model) (ICRP 106)
	¹²³ I-sodium iodo hippurate	53	Normal renal function	123I-sodium iodo hippurate (normal renal function) (ICRP 53)
			Abnormal renal function	123I-sodium iodo hippurate (abnormal renal function) (ICRP 53)
			Left kidney blockage	123I-sodium iodo hippurate (left kidney blockage) (ICRP 53)
			Right kidney blockage	123I-sodium iodo hippurate (right kidney blockage) (ICRP 53)
	¹²³ I-MIBG	53	—	123I-MIBG (ICRP 53)
	¹²³ I-monoclonal antibodies	106	Intact antibody	123I-monoclonal antibodies (intact antibody) (ICRP 106)
			F(ab') ₂ fragments	123I-monoclonal antibodies (F(ab') ₂ fragments) (ICRP 106)
			F(ab') fragments	123I-monoclonal antibodies (F(ab') fragments) (ICRP 106)
¹²⁴ I	¹²⁴ I-iodide	53	Thyroid blocked, uptake 0%	124I-iodide (thyroid blocked, uptake 0%) (ICRP 53)
			Thyroid uptake 5%	124I-iodide (thyroid uptake 5%) (ICRP 53)
			Thyroid uptake 15%	124I-iodide (thyroid uptake 15%) (ICRP 53)
			Thyroid uptake 25%	124I-iodide (thyroid uptake 25%) (ICRP 53)
			Thyroid uptake 35%	124I-iodide (thyroid uptake 35%) (ICRP 53)
			Thyroid uptake 45%	124I-iodide (thyroid uptake 45%) (ICRP 53)
			Thyroid uptake 55%	124I-iodide (thyroid uptake 55%) (ICRP 53)
¹³¹ I	¹³¹ I-iodide	53	Thyroid blocked, uptake 0%	131I-iodide (thyroid blocked, uptake 0%) (ICRP 53)
			Thyroid uptake 5%	131I-iodide (thyroid uptake 5%) (ICRP 53)
			Thyroid uptake 15%	131I-iodide (thyroid uptake 15%) (ICRP 53)
			Thyroid uptake 25%	131I-iodide (thyroid uptake 25%) (ICRP 53)
			Thyroid uptake 35%	131I-iodide (thyroid uptake 35%) (ICRP 53)
			Thyroid uptake 45%	131I-iodide (thyroid uptake 45%) (ICRP 53)
			Thyroid uptake 55%	131I-iodide (thyroid uptake 55%) (ICRP 53)
	¹³¹ I-sodium iodo hippurate	53	Normal renal function	131I-sodium iodo hippurate (normal renal function) (ICRP 53)
			Abnormal renal function	131I-sodium iodo hippurate (abnormal renal function) (ICRP 53)
			Left kidney blockage	131I-sodium iodo hippurate (left kidney blockage) (ICRP 53)
			Right kidney blockage	131I-sodium iodo hippurate (right kidney blockage) (ICRP 53)
	131I-MIBG	53	—	131I-MIBG (ICRP 53)
	¹³¹ I-monoclonal antibodies	106	Intact antibody	131I-monoclonal antibodies (intact antibody) (ICRP 106)
			F(ab') ₂ fragments	131I-monoclonal antibodies (F(ab') ₂ fragments) (ICRP 106)
			F(ab') fragments	131I-monoclonal antibodies (F(ab') fragments) (ICRP 106)
	¹³¹ I-norcholesterol	53	—	131I-norcholesterol (ICRP 53)
²⁰¹ Tl	²⁰¹ Tl-ion	106	—	201Tl-ion (ICRP 106) (ICRP 106)

Appendix D.

Masses and weighting factors between organ wall and content for five hollow organs: gallbladder, heart, small intestine, stomach and urinary bladder.

Gallbladder				
	Mass of organ content (g)	Mass of organ wall (g)	Weighting factor for the organ content (%)	Weighting factor for the organ wall (%)
Newborn	2.8	0.5	0.85	0.15
1-y-old	8	1.4	0.85	0.15
5-y-old	15	2.6	0.85	0.15
10-y-old	26	4.4	0.86	0.14
15-y-old female	42	7.3	0.85	0.15
15-y-old male	45	7.7	0.85	0.15
Adult female	48	8	0.86	0.14
Adult male	58	10	0.85	0.15
Heart				
	Mass of organ content (g)	Mass of organ wall (g)	Weighting factor of organ content (%)	Weighting factor of organ wall (%)
Newborn	26	20	0.57	0.43
1-y-old	48	50	0.49	0.51
5-y-old	135	85	0.61	0.39
10-y-old	230	140	0.62	0.38
15-y-old female	320	220	0.59	0.41
15-y-old male	430	230	0.65	0.35
Adult female	370	250	0.60	0.40
Adult male	510	310	0.62	0.38
Small intestine				
	Mass of organ content (g)	Mass of organ wall (g)	Weighting factor of organ content (%)	Weighting factor of organ wall (%)
Newborn	56	30	0.65	0.35
1-y-old	93	85	0.52	0.48
5-y-old	117	220	0.35	0.65
10-y-old	163	370	0.31	0.69
15-y-old female	280	520	0.35	0.65
15-y-old male	280	520	0.35	0.65
Adult female	280	600	0.32	0.68
Adult male	350	650	0.35	0.65
Stomach				
	Mass of organ content (g)	Mass of organ wall (g)	Weighting factor of organ content (%)	Weighting factor of organ wall (%)
Newborn	40	7	0.85	0.15
1-y-old	67	20	0.77	0.23
5-y-old	83	50	0.62	0.38
10-y-old	117	85	0.58	0.42
15-y-old female	200	120	0.63	0.38
15-y-old male	200	120	0.63	0.38
Adult female	230	140	0.62	0.38
Adult male	250	150	0.63	0.38

(Continued.)

Gallbladder				
	Mass of organ content (g)	Mass of organ wall (g)	Weighting factor for the organ content (%)	Weighting factor for the organ wall (%)
Urinary bladder				
	Mass of organ content (g)	Mass of organ wall (g)	Weighting factor of organ content (%)	Weighting factor of organ wall (%)
Newborn	10	4	0.71	0.29
1-y-old	11	9	0.55	0.45
5-y-old	61.7	16	0.79	0.21
10-y-old	98.4	25	0.80	0.20
15-y-old	134.1	35	0.79	0.21
female				
15-y-old male	153.3	40	0.79	0.21
Adult female	200	40	0.83	0.17
Adult male	200	50	0.80	0.20

ORCID iDs

Daphnée Villoing  <https://orcid.org/0000-0003-1437-2211>

Tae-Eun Kwon  <https://orcid.org/0000-0002-7252-4634>

Elisa Pasqual  <https://orcid.org/0000-0001-7181-6160>

Cari M Kitahara  <https://orcid.org/0000-0001-6416-4432>

Choonsik Lee  <https://orcid.org/0000-0003-4289-9870>

References

- Andersson M, Johansson L, Eckerman K and Mattsson S 2017 IDAC-Dose 2.1, an internal dosimetry program for diagnostic nuclear medicine based on the ICRP adult reference voxel phantoms *EJNMMI Res* **7** 88
- Andersson M, Johansson L, Minarik D, Mattsson S and Leide-Svegborn S 2014 An internal radiation dosimetry computer program, IDAC 2.0, for estimation of patient doses from radiopharmaceuticals *Radiat Prot Dosimetry* **162** 299–305
- Brix G, Nekolla E A, Borowski M and Noßke D 2014 Radiation risk and protection of patients in clinical SPECT/CT *Eur. J. Nucl. Med. Mol. Imaging* **41** 125–36
- Gomes Marin J F, Nunes R F, Coutinho A M, Zaniboni E C, Costa L B, Barbosa F G, Queiroz M A, Cerri G G and Buchpiguel C A 2020 Theranostics in nuclear medicine: emerging and re-emerging integrated imaging and therapies in the era of precision oncology *Radiographics* **40** 1715–40
- Goorley T et al 2016 Features of MCNP6 *Ann. Nucl. Energy* **87** 772–83
- ICRP 2009 Adult reference computational phantoms *ICRP Publication 110, Ann. ICRP* **39** 1–166
- ICRP 2002 Basic anatomical and physiological data for use in radiological protection : reference values *ICRP publication 89, Ann. ICRP* **32** 1–277
- ICRP 2010 Conversion coefficients for radiological protection quantities for external radiation exposures *ICRP Publication 116, Ann. ICRP* **40** 1–258
- ICRP 2006 Human alimentary tract model for radiological protection *ICRP publication 100, Ann. ICRP* **36** 1–336
- ICRP 2008a Nuclear decay data for dosimetric calculations *ICRP publication 107, Ann. ICRP* **38** 1–96
- ICRP 2020 Paediatric reference computational phantoms *ICRP Publication 143, Ann. ICRP* **49** 1–297
- ICRP 1998a Radiation dose to patients from radiopharmaceuticals *ICRP publication 53, Ann. ICRP* **28** 1
- ICRP 2008b Radiation dose to patients from radiopharmaceuticals - addendum 3 to ICRP publication 53 *ICRP Publication 106, Ann. ICRP* **38**
- ICRP 1998b Radiation dose to patients from radiopharmaceuticals (Addendum to ICRP publication 53) *ICRP Publication 80, Ann. ICRP* **28**
- ICRP 2016 The ICRP Computational Framework for internal dose assessment for reference adults: specific absorbed fractions *Ann. ICRP* **45** 1–74
- Indrakanti S, Li X and Rehani M M 2022 Patients undergoing multiple 18F-FDG PET/CT exams: assessment of frequency, dose and disease classification *Br. J. Radiol.* **95** 20211225
- Lee C, Lodwick D, Hurtado J, Pafundi D, Williams J L and Bolch W E 2010 The UF family of reference hybrid phantoms for computational radiation dosimetry *Phys. Med. Biol.* **55** 339–63
- Loevinger R, Budinger T F, Thomas F and Watson E E 1991 *MIRD Primer for Absorbed Dose Calculations revised edition* (New York: Society of Nuclear Medicine)
- NCRP 2009 *Ionizing Radiation Exposure of the Population of the United States* (Bethesda, MD: National Council on Radiation Protection and Measurement)
- NCRP 2019 *Medical Radiation Exposure of Patients in the United States* Online: <https://ncrponline.org/shop/reports/report-no-184-medical-radiation-exposure-of-patients-in-the-united-states-2019/>
- Stabin M and Farmer A 2012 OLINDA/EXM 2.0: The new generation dosimetry modeling code *J. Nucl. Med.* **53** 585
- Villoing D, Cuthbert T A, Kitahara C M and Lee C 2020 NCINM: organ dose calculator for patients undergoing nuclear medicine procedures *Biomed. Phys. Eng. Express* **6** 055010
- Xu X G 2014 An exponential growth of computational phantom research in radiation protection, imaging, and radiotherapy: a review of the fifty-year history *Phys. Med. Biol.* **59** R233–302
- Yordanova A, Eppard E, Kürpig S, Bundschuh R A, Schönberger S, Gonzalez-Carmona M, Feldmann G, Ahmadzadehfar H and Essler M 2017 Theranostics in nuclear medicine practice *Onco Targets Ther* **10** 4821–8